

# Low Ti Additions to Stabilize Ru-Ir Electrocatalysts for the Oxygen Evolution Reaction

Leopold Lahn,<sup>[a, b]</sup> Andrea M. Mingers,<sup>[c]</sup> Alan Savan,<sup>[d]</sup> Alfred Ludwig,<sup>[d]</sup> and Olga Kasian<sup>\*[a, b]</sup>

Anodic oxygen evolution reaction (OER) challenges large scale application of proton exchange membrane water electrolyzers (PEMWE) due to sluggish kinetics, high overpotential and extremely corrosive environment. While Ir oxides currently provide the best balance between activity and stability, the scarcity of Ir and corresponding high market price lead to poor cost-benefit factors. Mixing Ir with more stable non-precious Ti reduces the noble metal loading and may implicate stabilization, while addition of more catalytically active Ru ensures a high reaction rate. Here, we examine the activity-stability behavior of Ru-Ir-Ti thin film material libraries with low Ti-

content under the OER conditions. The high sensitivity to the dissolution of the individual alloy components was achieved by using online and off-line inductively coupled plasma mass spectrometry (ICP-MS) analysis. Our data reveal that even low Ti additions improve the stability of Ru-Ir catalysts without sacrificing activity. In particular, 5 at.% of Ti enable stability increase of Ir in the Ru-Ir catalyst by a factor of 3. Moreover, this catalyst exhibits higher activity compared to the Ti-free Ru-Ir alloys with similar Ir content. Observed activity-stability trends are discussed in light of X-ray photoelectron spectroscopy data.

## Introduction

The world's growing energy demand and the concomitant rise in greenhouse gas emissions due to fossil fuel-based energy production is associated with a plentitude of severe ecological and economic crises. Hence, the significance of energy production by renewable sources (like solar-, wind- and hydro-power) has progressively grown over the last decades. Yet, energy production from these sustainable sources suffers from instability due to natural intensity variations.<sup>[1,2]</sup> To tackle this challenge, environmentally friendly energy storage strategy is urgently needed. Hydrogen, produced by water electrolysis using surplus power from renewables, can serve as suitable

energy carrier, since it can cover the energy demand in multiple sectors. Success of the wide-spread application of proton exchange membrane water electrolysis (PEMWE) for on-site hydrogen production relies on the balance between cost and efficiency. The main bottleneck, in this sense, is the oxygen evolution reaction (OER) that requires high anodic potential, has sluggish kinetics and creates highly corrosive conditions.<sup>[3-6]</sup> Consequently, up to now only scarce noble metal catalysts can provide long term stability towards the OER.


Over the last 5 decades, significant research efforts have been made to find a suitable OER catalyst, which could ensure high electrical conductivity, electrocatalytic activity (low OER overpotential) and stability in acidic environments.<sup>[3,7-9]</sup> The detrimentally high positive potential during the OER leads to degradation and oxidation of catalyst materials and consequently the overpotential further increases with time.<sup>[4,7,9,10]</sup> Stability of different catalysts can be evaluated by several approaches ranging from accelerated degradation tests to direct measurements of their dissolution. Comparison of electrocatalytic activities of materials is rather based on correlative approaches, considering that activity is governed by a group of factors that can be distinguished into chemical and structural. The most common way of electrocatalytic activity prediction is based on correlation between the overpotential and the standard enthalpy for the transition to higher oxidation state.<sup>[5,7,11,12]</sup> In line with Sabatier's principle, metal oxides reveal a volcano-shaped relation between these two properties. The OER mechanism comprises several intermediate steps including the formation of hydroxyl radicals, their adsorption/desorption and steps of electron transfer.<sup>[3,5,7,11,12]</sup> The activity of materials that are less prone to oxidation is limited because of too weak adsorption of the oxygen-containing intermediates to the electrode surface. Conversely, electrodes that readily oxidize, bind the intermediates too strongly, which as well results in high overpotential.<sup>[5,7,11,12]</sup> Hence, the best catalytic activity is


[a] L. Lahn, Prof. Dr. O. Kasian  
Helmholtz-Zentrum Berlin GmbH, Helmholtz Institut Erlangen-Nürnberg  
Cauerstr. 1  
91058 Erlangen, Germany  
E-mail: olga.kasian@helmholtz-berlin.de

[b] L. Lahn, Prof. Dr. O. Kasian  
Department of Materials Science and Engineering  
Friedrich-Alexander-Universität Erlangen-Nürnberg  
91058, Erlangen, Germany

[c] A. M. Mingers  
Max-Planck-Institut für Eisenforschung GmbH  
Max-Planck-Straße 1  
40237 Düsseldorf, Germany

[d] A. Savan, Prof. Dr. A. Ludwig  
Materials Discovery and Interfaces, Institut für Werkstoffe  
Ruhr-Universität Bochum  
Gebäude IC 03/225  
44780 Bochum, Germany

 Supporting information for this article is available on the WWW under <https://doi.org/10.1002/celec.202300399>

 © 2023 The Authors. ChemElectroChem published by Wiley-VCH GmbH. This is an open access article under the terms of the Creative Commons Attribution License, which permits use, distribution and reproduction in any medium, provided the original work is properly cited.

expected in materials that adsorb these intermediates, or more generally oxygen species, neither too weakly, nor too strongly. Conductivity of oxides should also be considered in catalytic activity predictions, since oxidation often leads to formation of semiconducting or even insulating phases. For the rare case of oxides with metallic conductivity, it was shown that the oxygen binding energy to the surface of rutile  $\text{RuO}_2$  and  $\text{OsO}_2$  is at this sweet spot, revealing high activity of these materials.<sup>[5,7,9,11–13]</sup> However, neither  $\text{OsO}_2$  nor  $\text{RuO}_2$  are sufficiently stable to sustain the highly corrosive conditions during OER. In terms of maintaining an adequate balance between activity and stability during OER,  $\text{IrO}_2$  electrodes proved to be the better choice within single metal oxide catalysts.<sup>[9,10,14–17]</sup> Significant research efforts have been recently aimed at combining the high activity of Ru with the excellent stability of Ir in mixed oxides or alloys.<sup>[9,14,18–26]</sup> Despite their superior stability, even Ir-based catalysts dissolve during the OER in time.<sup>[9,10,17,27–29]</sup> Considering the undersupply of Ir and Ru and the corresponding high price on the market, even negligible dissolution may become challenging in the long term, shifting the research interest towards reduction of noble metal loading and stabilization while maintaining the high activity. To achieve these goals simultaneously, mixing Ir with more stable non-precious metal oxides of e.g. Ti and Sn was employed.<sup>[30–35]</sup> Yet, such an approach implies drawbacks in terms of activity, typically assigned to the reduction of active sites and formation of semiconductive or even insulating  $\text{TiO}_2$  and  $\text{SnO}_2$ .<sup>[8,34,36,37]</sup> Hence, the development of mixtures that maintain beneficial properties of both components demands control over electronic structure/oxidation state and the determination of the right mixing ratio. In fact, our recent investigations on Ir/TiOx thin films showed, that up to 50 at.% Ir can be replaced by  $\text{TiO}_x$ , without sacrificing activity while maintaining the stability of pure  $\text{IrO}_2$ .<sup>[34]</sup> Addition of catalytically more active elements, e.g. Ru, can improve the reactivity of such mixtures even more. Ideally, these active elements should also be stabilized by the non-precious metal, like in  $(\text{IrRuSn})\text{O}_2$ ,<sup>[38]</sup>  $(\text{IrRuTa})\text{O}_2$ ,<sup>[39]</sup> catalyst or in dimensionally stable anode (DSA)  $(\text{IrRuTi})\text{O}_2$  for the chlorine evolution reaction.<sup>[40–48]</sup> The number of research works on the performance of ternary alloy catalysts during the OER is rather limited. Moreover, often used in literature experimental approach to assessing the stability of OER catalysts, comprised the chronopotentiometry and analysis of current-potential curves during accelerated degradation tests. Though this method provides a good comparative basis on the possible service life of different catalysts, information on the origin of any instability remains unknown, since it is impossible to distinguish between several dissolution mechanisms.

Here, we were inspired by the idea of improving the stability of Ru-Ir anodes for the OER by introducing low amounts of Ti (1 to 6 at.%). The catalysts were synthesized as ternary Ru-Ir-Ti thin film material libraries with Ir contents below 50 at.% and screened for the electrocatalytic and dissolution properties using online ICP-MS. This approach provided the synchronized acquisition of activity-stability data with high sensitivity to dissolution of the individual alloy components. After initial screening, the long-term stabilities of the most

promising alloy compositions were tested at a current density of  $25 \text{ mA cm}^{-2}$  for ca. 28 h. The data on electrocatalytic performance were complemented by investigation of the electronic structure using X-ray photoelectron spectroscopy (XPS).

## Results

The details on preparation of the material libraries and initial characterization are described in the experimental section. Considering that electrocatalytic properties are only defined by the topmost surface layers of the alloys, all compositions mentioned in this work refer to surface compositions derived from XPS analysis. Figure 1 shows narrow scans of the Ir 4f (a), Ru 3d (b), Ti 2p (c) and O 1s (d) core levels for investigated compositions in the Ru-Ir-Ti libraries. Solid lines in Figure 1 represent the XP spectra measured on the pristine samples. Obtained data shows that Ir 4f<sub>7/2</sub> and Ru 3d<sub>5/2</sub> peaks are positioned at 60.3 eV and 279.6 eV, respectively, which according to literature corresponds to metallic states of Ir<sup>[49–51]</sup> and Ru.<sup>[49,52,53]</sup> The Ti 2p core level exhibits two contributions in the Ti 2p<sub>3/2</sub> peak for all investigated samples. The first at 453.9 eV can be assigned to metallic Ti,<sup>[54]</sup> while second at 457.6 eV corresponds to the oxidation state of Ti<sup>+4</sup>, e.g. in  $\text{TiO}_2$ .<sup>[50,54]</sup> The broad peak at about 462 eV observed in the region of the Ti 2p core level corresponds to overlapping Ti 2p<sub>1/2</sub> and Ru 3p<sub>3/2</sub> peaks. For all selected compositions deconvolution of the O 1s spectra (Figure 1d) shows contributions from lattice oxygen at about 529.4 eV, OH-groups at 530.8 eV and oxygen in water molecules at about 532.2 eV. Presence of lattice oxygen in pristine alloys can result from exposure of the samples to air and goes in line with the observed contribution of Ti oxides in Figure 1c.

The XPS data of the samples after a short anodic polarization under the OER are displayed by dotted curves in Figure 1. Compared to the pristine state, an increase of the Ir/Ru ratios is observed, indicating enrichment of the surface by Ir. The peak positions of Ir and Ru do not change, which indicates that they are mainly present in their metallic states. However, broadening of the Ir and Ru peaks after anodic polarization is observed, suggesting their partial oxidation. After polarization, the Ti signal is very weak, which makes quantification difficult due to the poor signal to noise ratio. Considering that the content of Ti was below 6 at.% in the pristine samples, even slight dissolution of Ti or segregation of Ir during anodic polarization would challenge the sensitivity of XPS towards the detection of Ti. The O 1s region shows changes in ratio between different oxygen species towards an increase in surface concentration of hydroxyl groups. Moreover, a shift of the OH peak by 0.4 eV towards higher binding energies can be observed. After exposing the alloy  $\text{Ru}_{0.62}\text{Ir}_{0.33}\text{Ti}_{0.05}$  for about 28 h to OER conditions at higher current density ( $25 \text{ mA cm}^{-2}$ ), the contribution from lattice oxygen increases (Figure S1). In addition, surface enrichment of Ir by 23 at.% is observed as a result of Ru and Ti depletion and the surface composition of the alloy is altered to  $\text{Ru}_{0.41}\text{Ir}_{0.56}\text{Ti}_{0.03}$ .

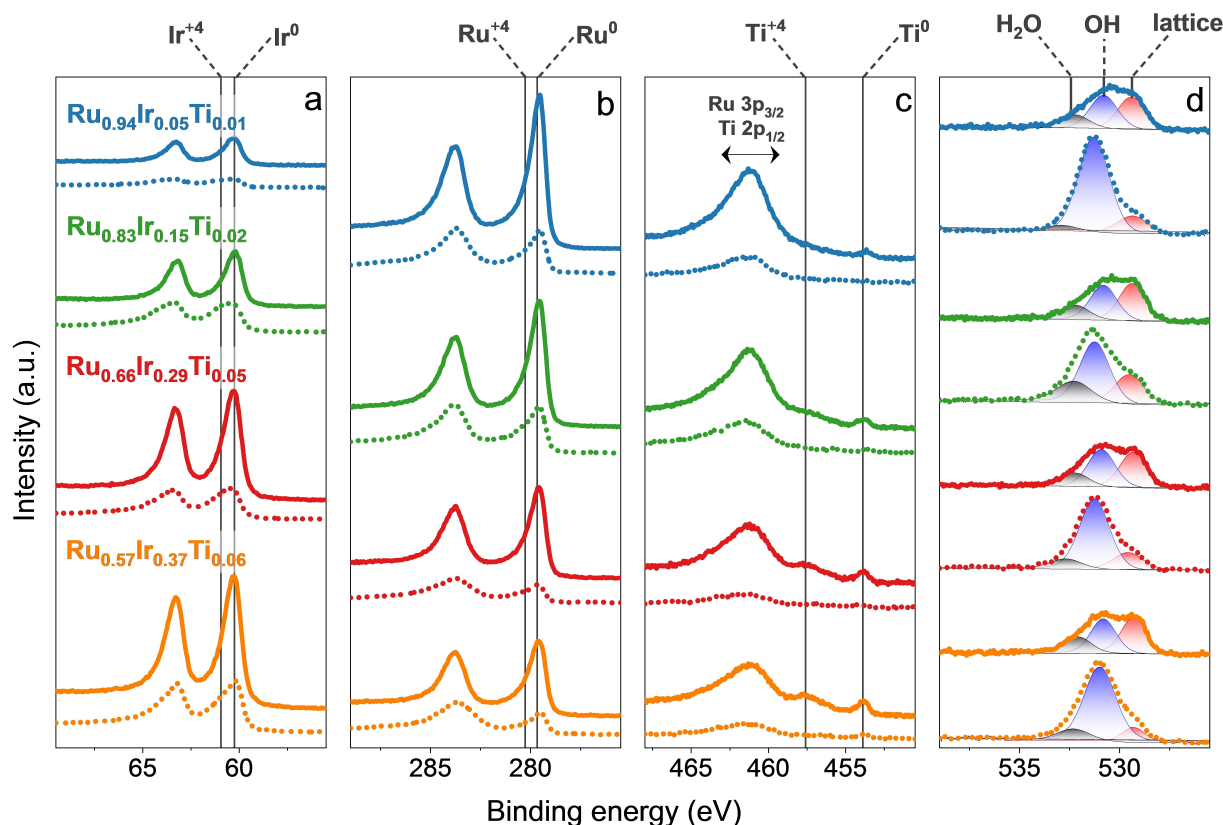


**Figure 1.** X-ray photoelectron spectra (XPS) of the Ir 4f (a), Ru 3d (b), Ti 2p (c) and O 1s (d) core levels of different Ru-Ir-Ti alloy compositions before (solid curves) and after (dotted curves) anodic polarization at  $1 \text{ mA cm}^{-2}$  for 2 min. The catalyst compositions are determined by integration of the Ru  $3d_{5/2}$ , Ir  $4f_{7/2}$  and Ti  $2p_{3/2}$  peaks. Vertical lines indicate the oxidation states of Ir, Ru and Ti in their metallic form ( $\text{Ir}^0$ ,  $\text{Ru}^0$  and  $\text{Ti}^0$ ) and in their oxides ( $\text{Ir}^{+4}$ ,  $\text{Ru}^{+4}$  and  $\text{Ti}^{+4}$ ). The overlap of the Ru  $3p_{3/2}$  with the Ti  $2p_{1/2}$  peaks is indicated in Figure 1c. Deconvolution of the O 1s spectra is indicated in Figure 1d and resulted in three peaks: lattice oxygen (red), OH groups (blue) and  $\text{H}_2\text{O}$  (grey).

For assessing electrocatalytic activity of different Ru-Ir-Ti alloys, anodic polarization curves are recorded for several selected compositions in the libraries as shown in Figure 2 (black curves). For comparison, identical measurements were performed on Ru-Ir alloys with similar Ir/Ru ratios (green curves). To assess benefits of the Ti addition, alloys with the same Ir content were chosen, considering that Ir is the most expensive component in such materials. Anodic polarization curves of pure Ru (blue curve) and Ir (red curve), recorded under identical electrochemical protocol, serve as benchmarks. The values of potential at a current density of  $5 \text{ mA cm}^{-2}$  were chosen as criteria for electrocatalytic activity. The activity of Ru-Ir-Ti alloys increases with increasing Ru content, and at Ru content of about 94 at.%, the activity approaches that of the benchmark Ru-electrode. The same trends are observed for Ru-Ir alloys, however, slightly higher Ru amounts in the Ru-Ir alloys and lack of non-active Ti, result in their generally better activities compared to Ru-Ir-Ti. The polarization curves obtained after 2 min holding Ru-Ir-Ti and Ru-Ir electrodes at  $1 \text{ mA cm}^{-2}$  are shown in Figure S2. After the OER, the activities slightly increase (up to 10 mV decrease of potential at  $5 \text{ mA cm}^{-2}$  for Ru-Ir-Ti and up to 20 mV for Ru-Ir), which can be explained by surface roughening and formation of amorphous hydrous oxide layers, providing additional active sites.<sup>[16,55–60]</sup>

The activity data presented in Figure 2 were measured online with dissolution of Ir, Ru and Ti using the SFC-ICP-MS setup. Figure 3 shows an example of such dissolution profiles for  $\text{Ru}_{0.66}\text{Ir}_{0.29}\text{Ti}_{0.05}$  (lower panels) as a response to an applied electrochemical protocol (upper panels). The curves in Figure 3a–c represent the electrochemical protocol for catalyst performance screening including an initial scan of potential from  $1.2 V_{\text{RHE}}$  to a potential corresponding to the current density of  $5 \text{ mA cm}^{-2}$  (Figure 3a), anodic polarization at  $1 \text{ mA cm}^{-2}$  for 2 min (Figure 3b) followed by an identical potential scan to evaluate possible alterations in activity and stability (Figure 3c). During the first anodic scan, the dissolution of Ir, Ru and Ti increases with increasing potential. As can be seen from the slopes of the dissolution curves, Ru shows the highest dissolution rates, followed by Ti and Ir. The same dissolution behavior is observed during the chronopotentiometric protocol in Figure 3b. The subsequent potential scan (Figure 3c) indicates an overall stability improvement by a factor of about 5, compared to the initial potential scan.

The quantification of the dissolved metal amounts can be revealed by integration of the dissolution profiles. Figure 4 shows the summarized data on dissolution of each element versus its content in the Ru-Ir-Ti (Figure 4a) and Ru-Ir alloys with similar Ir/Ru ratios (Figure 4b) during the anodic scans meas-

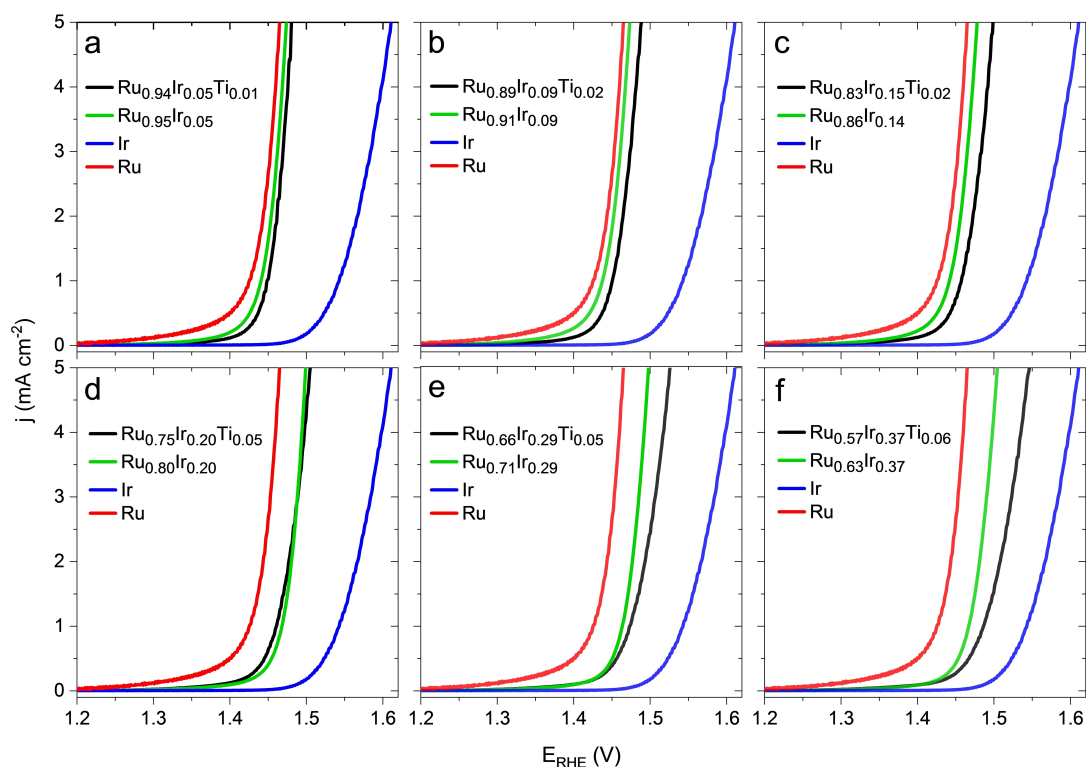


**Figure 2.** Activity trends of different Ru-Ir-Ti (black) and Ru-Ir (green) alloy compositions. The polarization curves of metallic Ru and Ir serve as benchmarks and are marked accordingly. The compositions of Ru-Ir alloys were chosen to match the content of Ir in Ru-Ir-Ti in all cases (a to f).

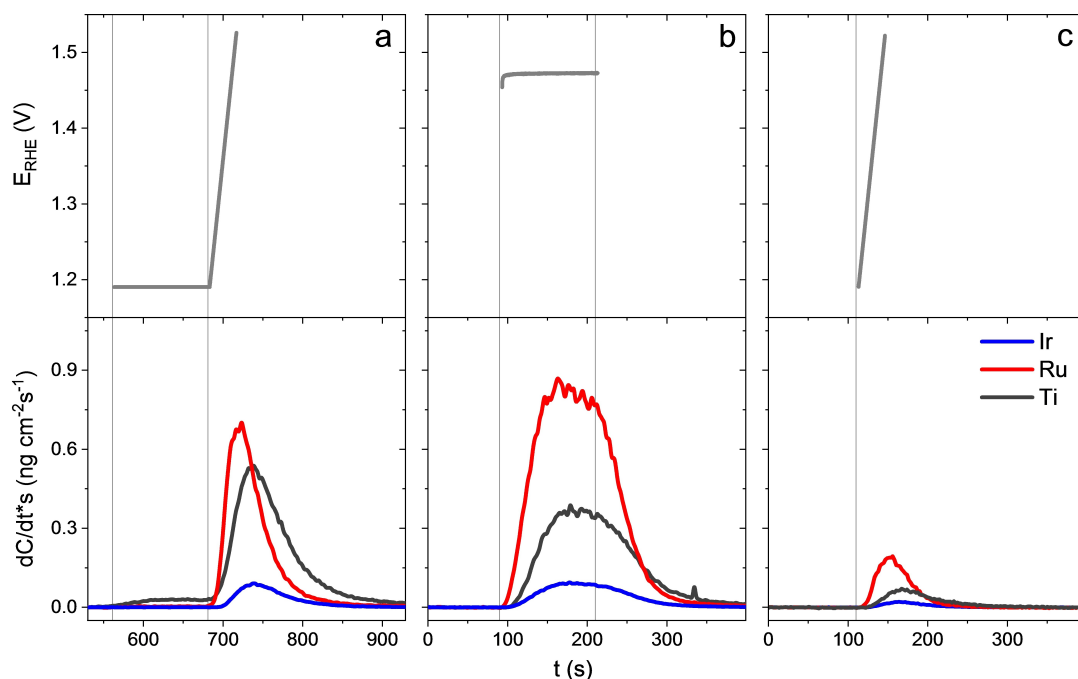


**Figure 3.** Dissolution rate curves as a response of an applied potential (a, c) or current (b) on a representative as-deposited  $\text{Ru}_{0.66}\text{Ir}_{0.29}\text{Ti}_{0.05}$  thin film alloy (a-c). Upper panels: the applied (a and c) and measured (b) potential as a function of time. Lower panels: corresponding dissolution rate curves of Ir (blue), Ru (red) and Ti (dark grey) as a function of time. The potential scans (a and c) are performed from  $1.2\text{V}_{\text{RHE}}$  to a potential corresponding to a current density of  $5\text{ mA cm}^{-2}$  at a scan rate of  $10\text{ mV s}^{-1}$ . The galvanostatic polarization (b) was performed at a current density of  $1\text{ mA cm}^{-2}$  for 2 min.

ured after polarization at  $1\text{ mA cm}^{-2}$  for 2 min. Such electrochemical pre-treatment is necessary to get rid of unstable

phases formed due to a contact of the electrode surface with air. This approach not only improves reproducibility, but also

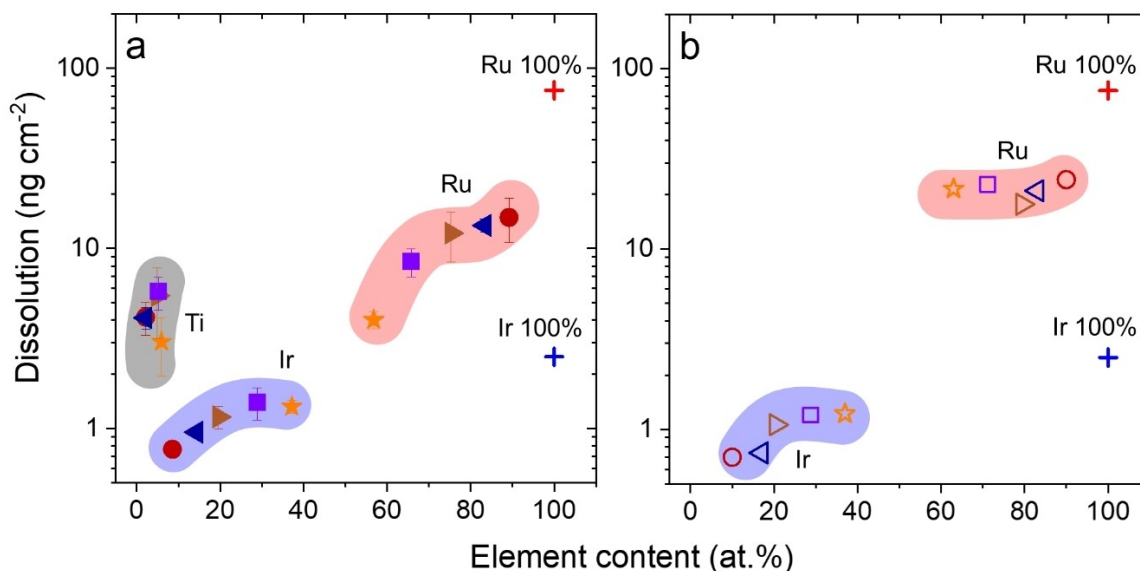


**Figure 4.** Dissolved metal amounts of iridium (Ir), ruthenium (Ru) and titanium (Ti) from different Ru-Ir-Ti (solid symbols in Figure 4a) and Ru-Ir alloys (hollow symbols in Figure 4b) with similar Ir/Ru ratios, obtained by integration of dissolution profiles after galvanostatic polarization at  $1 \text{ mA cm}^{-2}$  for 2 min. The dissolution data of metallic ruthenium (Ru 100%) and iridium (Ir 100%) are added as reference. Each symbol represents one alloy composition. As an example, the yellow star in Figure 4a represents the alloy composition  $\text{Ru}_{0.57}\text{Ir}_{0.37}\text{Ti}_{0.06}$  and in Figure 4b  $\text{Ru}_{0.63}\text{Ir}_{0.37}$ . Please note that the y-axis is presented in the logarithmic scale.

renders the comparison between different materials more conclusive. Dissolution data obtained on pristine surfaces can be found in Figure S3. Note that each symbol in Figure 4 represents one alloy composition. In line with previous reports,<sup>[9,15]</sup> the dissolution of the benchmark Ru electrode during the scan after electrochemical treatment equals to  $76 \text{ ng cm}^{-2}$ , while only  $3 \text{ ng cm}^{-2}$  of Ir benchmark was dissolved under the identical protocol. Within all investigated Ru-Ir-Ti and Ru-Ir alloy compositions, dissolution of both Ru and Ir from the alloys is lower than these benchmark values. The dissolution of Ir, Ru and Ti reflects the trend observed in the dissolution profiles in Figure 3, with Ru showing lower stability, followed by Ti and Ir. Moreover, dissolution of each component increases proportionally to its initial content in the alloy. For the binary as well as ternary alloys with Ir amounts above 30 at.%, a plateau in Ir dissolution values is noticed, indicating that maximum Ir stability is reached around this value. Hence, alloy compositions with Ir amounts of approximately 30 at.% ( $\text{Ru}_{0.62}\text{Ir}_{0.33}\text{Ti}_{0.05}$  and  $\text{Ru}_{0.67}\text{Ir}_{0.33}$ ) were chosen for further long-term performance evaluation. Comparison of Ir dissolution from the treated alloys with identical Ir amounts, for example  $\text{Ru}_{0.57}\text{Ir}_{0.37}\text{Ti}_{0.06}$  (solid yellow star in Figure 4a) and  $\text{Ru}_{0.63}\text{Ir}_{0.37}$  (hollow yellow star in Figure 4b), reveals that Ir dissolution from both binary and ternary alloys is about  $1 \text{ ng cm}^{-2}$ . In contrast, Ru dissolution from the binary alloy is more than five times higher than that from the ternary alloy. Next to the stabilizing effect of Ti, which was reported before,<sup>[32,34,35]</sup> the slightly lower Ru amount in the Ru-Ir-Ti alloys is also responsible for lower Ru dissolution. Still, the 6 at.% lower Ru amount in  $\text{Ru}_{0.57}\text{Ir}_{0.37}\text{Ti}_{0.06}$  is unlikely to be the only reason for the 5-fold lower Ru dissolution compared to that in  $\text{Ru}_{0.63}\text{Ir}_{0.37}$ .

To assess the stability of Ru-Ir-Ti on an extended timescale, an H-cell setup with divided anodic and cathodic compartments was employed. Dissolution was measured by frequently taking electrolyte samples from the anodic compartment and their offline analysis by the ICP-MS. The lower panels in Figure 5 compare Ir and Ru dissolution curves between a binary  $\text{Ru}_{0.67}\text{Ir}_{0.33}$  alloy (Figure 5a) and ternary  $\text{Ru}_{0.62}\text{Ir}_{0.33}\text{Ti}_{0.05}$  (Figure 5b) with same Ir amounts during anodic polarization at  $25 \text{ mA cm}^{-2}$  for ca. 28 h. The upper panels in Figure 5 represent the potential – time dependence while holding at  $25 \text{ mA cm}^{-2}$ . The stability behavior of the electrodes follows a similar trend as in online experiments, with Ru showing the highest dissolution, followed by that of Ti (in the case of the ternary alloy) and Ir. During the first 200 min, a significant increase in Ir and Ru dissolution is observed in both alloys. Ru dissolution reaches steady-state after about 1000 min and at the end of the experiment both alloys reveal similar dissolution values around  $50 \text{ } \mu\text{g cm}^{-2}$ . In contrast to the comparable Ru dissolution, Ir dissolution in  $\text{Ru}_{0.62}\text{Ir}_{0.33}\text{Ti}_{0.05}$  ( $2.8 \text{ } \mu\text{g cm}^{-2}$ ) is more than 3 times lower compared to  $\text{Ru}_{0.67}\text{Ir}_{0.33}$  ( $9.3 \text{ } \mu\text{g cm}^{-2}$ ), though the steady state was not reached in both cases. The dissolution of Ti in the Ru-Ir-Ti alloy (Figure 5b) approaches a value of  $5.0 \text{ } \mu\text{g cm}^{-2}$  at the end of the experiment. Figure 5 shows higher activity and more stable performance of the ternary alloy compared to the binary alloy. The anodic polarization curve of  $\text{Ru}_{0.62}\text{Ir}_{0.33}\text{Ti}_{0.05}$  recorded after the H-cell experiment is shown in Figure 5c together with the polarization curve recorded on the pristine sample. The long-term OER exposure leads to 10 mV decrease of potential at a current density of  $5 \text{ mA cm}^{-2}$ . A slight increase of the background current density at potentials below the OER (compared to the polarization curve for pristine alloy) indicates

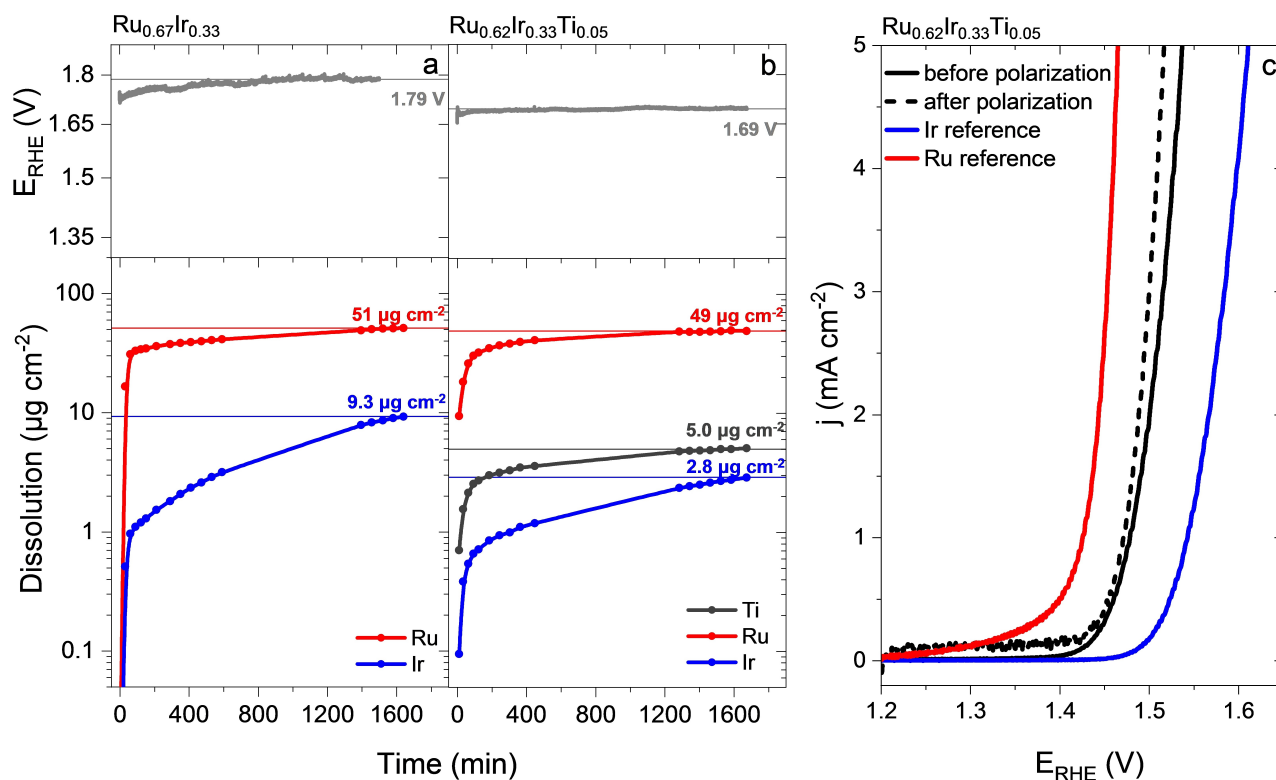


**Figure 5.** Comparison of long-term performance between Ru-Ir and Ru-Ir-Ti alloys. Upper panels: measured potential during anodic polarization of a representative binary  $\text{Ru}_{0.67}\text{Ir}_{0.33}$  alloy (a) and the ternary  $\text{Ru}_{0.62}\text{Ir}_{0.33}\text{Ti}_{0.05}$  alloy (b) at same Ir amounts during anodic polarization at  $25 \text{ mA cm}^{-2}$  for 28 hours. The values of potential at the end of the experiment are noted in the Figures. Lower panels: Corresponding iridium (Ir), ruthenium (Ru) and titanium (Ti) dissolution. The dissolution values of iridium, ruthenium and titanium at the end of the experiment are noted in the Figures. c: anodic polarization curves before (solid black) and after the polarization (dashed black) of the ternary  $\text{Ru}_{0.62}\text{Ir}_{0.33}\text{Ti}_{0.05}$  alloy. Polarization curves of benchmark iridium (blue) and ruthenium (red) are included.

increase of the surface area, probably due to hydrous oxide formation.

## Discussion

Exploiting the high OER activity of Ru and excellent stability of Ir, by mixing these elements in alloys or binary oxides, has been investigated for almost five decades.<sup>[4,9,18–20,22,25,61]</sup>  $\text{RuO}_2$  was reported to have exceptional activity with an overvoltage of 0.2 V.<sup>[62]</sup> Several studies on the catalytic properties of  $\text{RuO}_2$  followed, as well as the electrochemical and kinetic investigations of  $\text{RuO}_2$  electrodes by Galizzioli et al.<sup>[63–64]</sup> However, the major drawback of Ru or  $\text{RuO}_2$  as an OER catalyst is the low stability in the very corrosive environment at the anode.<sup>[9,14,17,49,65–67]</sup> Based on XPS studies, Kötzt et al.<sup>[49,67]</sup> reported the formation of a hydrous  $\text{RuO}_x$  layer as a result of corrosion and presented a model of the OER (and corrosion) of Ru and  $\text{RuO}_2$  electrodes. Strategies were developed to stabilize Ru by mixing or alloying with other precious or non-precious elements. In the beginning of the 1980s, research was pushed towards mixing/alloying Ru or  $\text{RuO}_2$  with Ir or  $\text{IrO}_2$  as the additions of Ir significantly increased stability while the increase in overpotential was small.<sup>[18–19,39,61]</sup> Despite the consensus that even small  $\text{IrO}_2$  admixtures significantly improve the stability of

$\text{RuO}_2$ , the stabilization mechanism is, still today, a matter of debate. Yet, catalyst stability is a pivotal element in developing efficient water electrolysis technologies. While some authors explain the stabilization of  $(\text{IrRu})\text{O}_2$  mixed oxides with changes in the electronic structure of Ir and Ru,<sup>[18–19]</sup> others explain it with Ir surface segregation.<sup>[9,14,20,22,68,69]</sup> However, even  $(\text{IrRu})\text{O}_2$  mixed oxides undergo dissolution and deterioration of activity with time.<sup>[9,10,15–17,27,28,69]</sup> It was shown that the activity of  $(\text{IrRu})\text{O}_2$  gradually approaches that of  $\text{IrO}_2$  as Ru progressively dissolves during the OER.<sup>[9,27,28]</sup> Kasian et al.<sup>[9]</sup> demonstrated, that the dissolution and corresponding removal of just a few percent of Ru from a monolayer of a  $(\text{IrRu})\text{O}_2$  mixed oxide surface leads to substantial penalties in the OER activity. For additional stabilization, Ir can be mixed with non-precious metals like Ti or Sn.<sup>[30–35,70–72]</sup> Besides an increase in service life, this leads to a reduced Ir content and therefore a lower cost. Such catalyst materials usually suffer from reduced activity due to the poor conductivity of stabilizing oxides, while success of their application relies on the determination of the right mixing ratio.<sup>[8,34,36,37]</sup> Our recent study showed, that up to 50% Ir can be replaced by  $\text{TiO}_x$  in  $\text{Ir/TiO}_x$  thin films without sacrificing catalytic activity.<sup>[34]</sup> This remarkable activity-stability relation was explained on the atomic scale, by the localized formation of Ir-Ti mixed oxides, where Ti provides stability and Ir the catalytically active sites.<sup>[34]</sup> For further enhancement of the utilization of Ir,

Ir-TiO<sub>x</sub> based nanocomposites provide promising features in terms of activity and stability. Loncar et al.,<sup>[70]</sup> for example, used the strong metal support interaction between Ir and TiON<sub>x</sub> and produced Ir/TiON<sub>x</sub>/C nanoparticles, offering about three times higher activity compared to a benchmark Ir Black catalyst. Van Pham et al. synthesized IrO<sub>2</sub>@TiO<sub>2</sub> core-shell particles that showed superior activity with inferior stability, compared to the commercial IrO<sub>2</sub>/TiO<sub>2</sub> catalyst.<sup>[71]</sup> In another study, IrO<sub>2</sub> nanoparticles dispersed in TiO<sub>2</sub>, revealed enhanced OER stability, while the activity increased by a factor of about 5 compared to commercial IrO<sub>2</sub>/TiO<sub>2</sub>.<sup>[72]</sup> Adding catalytically more active elements, like Ru, to such Ir-non-precious metal mixtures can furthermore enhance the rate of the OER. Hutchings et al., for example, investigated (IrRuSn)O<sub>2</sub> mixed oxides and compared their electrocatalytic properties and microstructure to that of binary (IrRu)O<sub>2</sub>, IrO<sub>2</sub> and RuO<sub>2</sub>.<sup>[38]</sup> Based on accelerated degradation tests, they reported a significant increase in lifetime and stable performance compared to pure IrO<sub>2</sub>, RuO<sub>2</sub> and (IrRu)O<sub>2</sub>, which they attributed to the formation of metastable (IrRuSn)O<sub>2</sub> phases.<sup>[38]</sup> Yeo et al. synthesized a ternary oxide, containing Ir, Ru and Ta (IrRuTa)O<sub>2</sub>.<sup>[39]</sup> They showed that Ta not only improves corrosion resistance in acidic environments, but also stabilizes the mixed Ru<sup>+3</sup>-Ru<sup>+4</sup> cationic valences that are attributed to more favorable electrocatalytic activity.<sup>[39]</sup> Surface properties of mixed oxides containing Ir, Ru and Ti were studied in the past regarding their considerable application in dimensionally stable anodes (DSAs) for the chlorine evolution reaction.<sup>[40–48]</sup> Kameyama et al. proved the formation of a rutile type mixed oxide between IrO<sub>2</sub>, RuO<sub>2</sub> and TiO<sub>2</sub>, and revealed interesting microstructural surface characteristics, like RuO<sub>2</sub> enrichment at internal surfaces (e.g. in cracks and pores) and TiO<sub>2</sub> enrichment at the external surface.<sup>[73]</sup> Active coatings of mixed oxides of Ir, Ru and Ti were studied by Gorodetskii and Neburchilov.<sup>[41,42,46–48]</sup> By optimizing the ratio between IrO<sub>2</sub>, RuO<sub>2</sub> and TiO<sub>2</sub>, they improved the corrosion resistance of (IrRuTi)O<sub>2</sub>.<sup>[48]</sup> Considering that composition of the catalyst strongly depends on the preparation conditions and evolution of the surface is dictated by the ongoing reaction and electrolysis parameters, the insights on surface composition and structure of (IrRuTi)O<sub>x</sub> gained for the chlorine evolution reaction cannot directly be transferred to their application in the OER. Although both reactions are anodic reactions, the OER is associated with higher catalyst corrosion and consequently massive changes in the catalyst's surface composition. This principally stems from the higher overpotential and the fact that oxygen evolution and catalyst corrosion share common intermediates.<sup>[27]</sup> In addition, the OER has slower kinetics compared to the chlorine evolution (four vs. two electron reaction mechanism<sup>[74]</sup>). As a result, the surface accommodates the reaction intermediates for longer times which has direct impact on the surface composition. Our XPS analysis of the Ru-Ir-Ti alloys at the core levels of Ir 4f, Ru 3p and Ti 2p (Figure 1) reveals metallic states of these elements<sup>[19,34,49–53,75,76]</sup> explaining high catalytic activity of the samples towards the OER. Change in the intensity ratios between the elements after polarization points towards restructuring of the surfaces, although no peak shift is observed (Table 1). For instance, for all investigated alloy compositions

**Table 1.** Iridium/ruthenium ratios calculated from XPS data in Figure 1 and the ratios between contributions from oxygen in OH groups and oxygen in an oxide lattice before and after anodic polarization of several alloy composition. All samples were polarized at 1 mA cm<sup>-2</sup> for 2 min in an 0.1 M HClO<sub>4</sub> electrolyte.

Composition	(Ir/Ru) <sub>bef.</sub>	(Ir/Ru) <sub>aft.</sub>	(O <sub>OH</sub> /O <sub>lattice</sub> ) <sub>bef.</sub>	(O <sub>OH</sub> /O <sub>lattice</sub> ) <sub>aft.</sub>
Ru <sub>0.94</sub> Ir <sub>0.05</sub> Ti <sub>0.01</sub>	0.06	0.11	1.44	5.73
Ru <sub>0.83</sub> Ir <sub>0.15</sub> Ti <sub>0.02</sub>	0.17	0.33	1.29	2.81
Ru <sub>0.66</sub> Ir <sub>0.29</sub> Ti <sub>0.05</sub>	0.44	0.93	1.42	4.59
Ru <sub>0.57</sub> Ir <sub>0.37</sub> Ti <sub>0.06</sub>	0.65	1.22	1.24	4.82

we observe Ir surface enrichment by up to 23 at.%. Comparing the Ir/Ru ratios before and after polarization (Table 1), one can see that the ratios almost consistently double after polarization. The reason behind this may be the formation of some stable phases at the surfaces as a result of dissolution and oxidation. It can be assumed that during polarization, Ru leaches out and an Ir enriched surface remains, providing higher stability. In fact, nano segregation of Ir in Ir-Ru alloys can be achieved via specific synthesis strategies aimed for better activity-stability relationships as was proposed by Danilovic et al.<sup>[14]</sup> In this work the synthesis strategy resulted in an Ir enriched surface protecting the underlying Ru layer from dissolution, interestingly without sacrificing activity.<sup>[14]</sup> This is rather counterintuitive as it could be expected that depletion of the more active Ru causes penalties in terms of catalytic activity. However, the increase in active surface area due to the formation of a porous hydrous IrO<sub>x</sub> layer may compensate the activity losses due to leaching of the more active Ru. Our results reveal a similar trend, as even the alloys subjected to the long-term performance tests for 28 h at a current density as high as 25 mA cm<sup>-2</sup> did not suffer from activity losses (Figure 5). Besides the increase in active surface area, the altered chemistry due to the presence of Ti can be another explanation for the maintenance or even increase in activity after polarization of the Ru-Ir-Ti alloys, which will be discussed in detail later. Still, for (IrRu)O<sub>2</sub> mixed oxide thin films it was shown that under OER conditions, the activity gradually approaches that of IrO<sub>2</sub>.<sup>[9]</sup> Moreover, a recent study on (IrRu)O<sub>2</sub> mixed oxide nanoparticles confirmed Ir surface segregation after thermal treatment and associated decline in activity but increase in stability.<sup>[77]</sup>

The Ti 2p spectra of the as prepared Ru-Ir-Ti alloys (Figure 1c) reveal contributions from TiO<sub>2</sub> at a binding energy of about 458 eV. Moreover, deconvolution of the O 1s spectra (Figure 1d) reveals the presence of lattice oxygen and OH groups. Considering the high oxygen affinity of Ti, it is very likely that some Ti on the alloy surfaces was oxidized by atmospheric oxygen, since the thin films were exposed to air. To illustrate the evolution of the catalytic surfaces after the OER, the O<sub>OH</sub>/O<sub>lattice</sub> ratios in O 1s spectra before and after anodic polarization are calculated and presented in Table 1. Interestingly, after the OER contributions from OH groups in O 1s spectra increase. Moreover, for the electrochemically treated samples we observe a 0.4 eV shift of the OH peak towards higher binding energies, which indicates alterations in the binding environment of the M-OH bonds and formation of

bonds between OH-species and metal with lower affinity for oxygen. Thus, formation of hydrous  $\text{IrO}_x$ ,  $\text{RuO}_x$  and/or  $(\text{IrRu})\text{O}_x$  species after anodic polarization can be concluded despite the absence of shifts in Ir and Ru peaks. Along with that, the slight broadening of the Ir 4f and Ru 3d peaks after polarization (Figure 1a and b) indirectly supports the suggestion of formation of Ir and Ru oxidized species. Still Ti has higher affinity for oxygen and it is more likely to bind oxygen during anodic polarization, inhibiting further oxidation of noble Ir and Ru. Hence, catalytic activity remains high, as the active Ir and Ru sites are maintained, providing an additional explanation for the conservation or even increase in activity of the Ru-Ir-Ti alloys after polarization. A similar trend was observed in Ir/TiOx catalysts in which metallic Ir species coexist with Ti-enriched oxide phases, leading to stabilization against dissolution without sacrificing activity.<sup>[34]</sup>

In most of the above-mentioned studies, stability of the catalysts was verified by accelerated degradation tests. So far, there was no systematic study which compared different Ru-Ir-Ti alloy compositions under identical conditions. Our approach allows selective measurements of dissolution rates for all components of numerous Ru-Ir-Ti compositions during the electrochemical experiment. To compare the stability of the investigated alloys with other Ir based catalysts, stability numbers (S-numbers) were estimated based on the electrochemical data shown in Figure 4 and Figure 5. The S-number was recently introduced by Geiger et al.<sup>[78]</sup> and is the amount of  $\text{O}_2$  molecules that are evolved per dissolved catalyst atom. Hence, the S-number is a metric for catalyst stability, which is independent from surface area, and in the case of nanoparticles, of catalyst loading.<sup>[78]</sup> S-numbers were estimated for the alloys polarized at  $25 \text{ mA cm}^{-2}$  (for more than 24 h) and  $1 \text{ mA cm}^{-2}$  (for 2 min).

Table 2 comprises the S-numbers of the Ru-Ir-Ti alloys polarized at  $25 \text{ mA cm}^{-2}$ , as well as those of other Ir-based materials from literature. Using the previously suggested approach for alloy catalysts,<sup>[79]</sup> S-numbers were estimated for Ir ( $S_{\text{Ir}}$ ) as well as Ru ( $S_{\text{Ru}}$ ), since both elements contribute to the OER. Estimation of the S-numbers for both Ir and Ru helps identifying the less stable metal alloy component, which is crucial for the development of dissolution mitigation strategies. Compared to pure Ir, the Ru-Ir-Ti alloys show 5–6 times higher  $S_{\text{Ir}}$ . This is remarkable, considering that the investigated alloys were polarized at a 25 times higher current density and about 300 times longer OER exposure compared to metallic Ir catalyst in the work of Geiger et al.<sup>[78]</sup> Presented here Ru-Ir-Ti alloys reveal up to 3 times higher  $S_{\text{Ir}}$  compared to Ru-Ir alloys with similar Ir/Ru ratios (Table 2). This increase in S-number indicates stabilization, which can be ascribed to the Ti additions, but also to the surface enrichment of the more stable Ir, which was observed in the XPS data (Figure 1 and Table 1).  $S_{\text{Ir}}$  of  $(\text{IrRu})\text{O}_2$  and  $(\text{IrTi})\text{O}_x$  mixed oxides that were investigated by Kasian et al.,<sup>[9,34]</sup> are almost one magnitude higher than those of the Ru-Ir-Ti alloys. This is because oxides are more stable towards the OER than metals. Besides that, the catalysts from references<sup>[9,34]</sup> were polarized at relatively mild conditions with a 25 times lower current density. Compared to  $\text{IrO}_2$ @ $\text{TiO}_2$  core-

**Table 2.** Compilation of stability numbers (S-numbers) of different Ir based catalysts in this work and literature.

Anode material	S-number Ir	S-number Ru	Conditions	Reference
$\text{Ru}_{0.66}\text{Ir}_{0.32}\text{Ti}_{0.02}$	$4.7 \times 10^5$	$2.0 \times 10^4$	0.1 M $\text{HClO}_4$ ; 28 h; $25 \text{ mA cm}^{-2}$	This work
$\text{Ru}_{0.62}\text{Ir}_{0.33}\text{Ti}_{0.05}$	$5.9 \times 10^5$	$3.4 \times 10^4$	0.1 M $\text{HClO}_4$ ; 28 h; $25 \text{ mA cm}^{-2}$	This work
$\text{Ru}_{0.67}\text{Ir}_{0.33}$	$1.8 \times 10^5$	$3.2 \times 10^4$	0.1 M $\text{HClO}_4$ ; 27 h; $25 \text{ mA cm}^{-2}$	This work
$\text{Ir}_{0.50}\text{Ti}_{0.50}\text{O}_x$	$1.5 \times 10^6$	–	0.1 M $\text{HClO}_4$ ; steady-state; $1 \text{ mA cm}^{-2}$	[34]
$\text{Ir}_{0.70}\text{Ru}_{0.30}\text{O}_2$	$1.0 \times 10^6$	$1.0 \times 10^5$	0.1 M $\text{HClO}_4$ ; 1 min; $1 \text{ mA cm}^{-2}$	[9,79]
$\text{IrO}_2$ @ $\text{TiO}_2$	$1 \times 10^4$	–	0.1 M $\text{HClO}_4$ ; 5 min; $100 \text{ mA mg}^{-1}$	[71]
Ir metal	$1.0 \times 10^5$	–	0.1 M $\text{HClO}_4$ ; 5 min; $1 \text{ mA cm}^{-2}$	[78]
$\text{IrO}_x$ (amorphous)	$5.0 \times 10^4$	–	0.1 M $\text{HClO}_4$ ; 5 min; $1 \text{ mA cm}^{-2}$	[78]
$\text{IrO}_2$	$9.2 \times 10^5$	–	0.1 M $\text{HClO}_4$ ; 10 min; $1 \text{ mA cm}^{-2}$	[78]

shell microparticles from reference,<sup>[71]</sup> the Ru-Ir-Ti alloys reveal S-numbers, which are more than one order of magnitude higher. However, having in mind the different structure and physical degradation mechanism of thin films and micro-/nanoparticles, their direct comparison is rather unfair. The stability numbers of Ir are about one order of magnitude higher than those of Ru, suggesting that Ru is the element mostly involved in the OER. This observation complements in general higher OER activity of Ru and the inverse relationship between activity and stability of monometallic OER electrocatalysts.<sup>[80]</sup> In addition, the differences in S-numbers suggest that the active Ir and Ru sites maintain their original properties in the alloys with respect to the OER mechanism, as indicated by Kasian et al.<sup>[9,79]</sup> However, in contrast to the observations of  $(\text{IrRu})\text{O}_2$  mixed oxides,<sup>[9,79]</sup> the activity of the Ru-Ir-Ti alloys remains the same or even slightly increases in time with the OER despite the surface enrichment of Ir (Figures 2, 5 and S2). This can be explained by an increase in electrochemically active surface area due to the formation of (hydrous) metal oxides with the OER and the change in chemistry due to the presence of Ti.

To illustrate differences in Ir and Ru dissolution from binary and ternary alloys with the same Ir content, we roughly estimated the number of dissolved atomic layers during the OER. The calculations were performed using the dissolution data from the H-cell experiments, the surface composition of the alloys assessed by XPS (Figure 1) and the atomic diameters and densities of Ir and Ru atoms in the lattice. More details



regarding the calculations can be found in the Supporting Information. As an example, under the same conditions of the OER, Ir dissolves from about 11 atomic layers of the  $\text{Ru}_{0.67}\text{Ir}_{0.33}$  alloy, whereas Ir dissolution from  $\text{Ru}_{0.62}\text{Ir}_{0.33}\text{Ti}_{0.05}$  is limited to only 3 atomic layers. The dissolution of Ru from these two alloys is comparable, namely 59 atomic layers are subjected to the dissolution from the ternary alloy and 57 from the binary alloy. Hence, long term experiments reveal that the stabilizing effect of Ti is rather restricted to Ir. This may be explained with the significant dissolution rate of Ru at high current density which exceeds the rate of oxidation, preventing formation of more stable mixed oxides phases. Yet, short-term SFC-ICP-MS experiments (Figure 4, Figure S3 and Figure S4) show a clear trend toward stabilization of Ru with increasing amount of Ti, compared to the Ti free Ru-Ir alloys. This reveals that predictions of the catalytic stability should always refer to the time scale of experiments. The S-numbers determined from the prior are up to two orders of magnitude higher than those of the H-cell experiments and literature values of other Ir containing catalysts (Table 2). As revealed by H-cell experiments on the long timescale, the dissolution rates do not reach steady state even after 24 h (Figure 5). Hence, it can be expected that the stability from the short term experiments is underestimated, since it relies on the initial dissolution rates in contrast to long term H-cell experiments. This result is in agreement with previous reports,<sup>[79]</sup> showing deviations between the S-numbers obtained from SFC- and H-cell setups. Besides stability, also the prediction of catalytic activity significantly relies on the experimental conditions and the chosen current density, as can be illustrated by comparing the electrochemical data from the SFC-ICP-MS (Figure 2 and Figure S2) and H-cell experiments (Figure 5). This is because the mechanisms of the OER and dissolution can change depending on current density, which makes comparison of catalytic properties of two different materials problematic. The evolution of potential during the long-term OER performance tests (upper panels in Figure 5) indicates significantly more stable performance of the Ru-Ir-Ti alloy. Furthermore, it presents higher activity compared to the Ti free Ru-Ir alloy with the same Ir content. Considering this, together with the 3 times lower Ir dissolution, it becomes clear that the investigated Ru-Ir-Ti alloys outperform Ru-Ir alloys. Although the S-numbers obtained during short-polarization (Figure S4) should not be used for benchmarking to other catalysts, they reinforce our finding of Ti-induced stabilization of Ir and Ru in Ru-Ir-Ti alloys, as they reveal an increase in Ir and Ru S-numbers with increasing Ti content. The reason for this stabilization can be, next to Ir surface enrichment, the formation of (hydrous) mixed oxides during polarization. Recently, the coexistence of metallic Ir in a  $\text{TiO}_x$  phase was proven on the atomic scale and related to the increase in stability of Ir-Ti mixed oxides of  $\text{IrO}_2$ , where Ir provides the catalytic activity and Ti the stability.<sup>[34]</sup> There are multiple indicators for the electrochemical formation of such (hydrous) mixed oxide phases on the surfaces of the investigated Ru-Ir-Ti alloys, starting with the increase of the OH peak in the O 1s spectra after polarization (Figure 1d). Having this and the slight broadening of the Ir 4f and Ru 3p peaks (Figure 1a and Figure 1b) in mind, it can be

presumed that these hydrous oxides contain Ir and, to some extent Ru. Another indicator for the formation hydrous oxides during polarization are the differences in activity and stability data before and after polarization (Figure 2, Figure S2 and Figure 5). Even after long term polarization at high current densities, the OER activity remains the same or even increases (Figure 5c). This is attributable to the electrochemical formation of hydrous oxides of Ir and Ru, resulting in an increase in surface area and the number of active sites. Moreover, the high affinity of Ti for oxygen implies that oxygen more likely binds to Ti during anodic polarization to form oxides, suppressing further oxidation of Ir and Ru. Having at least some portions of metallic Ir and Ru stabilized at the surface would provide an additional explanation for the stability increase without the sacrifice of catalytic activity.

## Conclusions

Activity-stability relationships of Ru-Ir-Ti thin film catalysts containing up to 5 at.% Ti were investigated. Our data show that the ternary alloys outperform binary Ru-Ir alloys in terms of activity and stability. The Ru-Ir-Ti alloy containing about 30 at.% Ir exhibits stable catalytic performance during 28 h of anodic polarization at  $25 \text{ mA cm}^{-2}$ , while only three atomic layers of the catalyst are affected by Ir dissolution. Opposed to that, the Ti-free Ru-Ir alloy with identical Ir content lost Ir from 11 atomic layers during the same performance tests. Calculated stability numbers indicate that Ti additions as low as 5 at.% boost Ir stability of Ru-Ir alloy catalysts by a factor of 3, and by a factor of 6 compared to pure Ir metal. XPS measurements suggest Ir surface enrichment and formation of Ir, Ru and Ti-containing hydrous oxides during the OER. These two effects may explain the observed stability boost without the sacrifice of catalytic activity. Further efforts will be aimed at understanding the origin of this improved stability by the surface- and near surface structure insights.

## Experimental Section

Ru-Ir-Ti and Ti-free Ru-Ir thin film libraries with similar Ru-Ir gradients were synthesized by combinatorial magnetron sputtering (CMS 400/600 LIN, DCA Instruments, Turku, Finland) employing a confocal co-deposition approach. Single crystal Si wafers (100) with a 140 nm barrier of thermal  $\text{SiO}_2$  against silicide formation, were used as substrates to prepare samples with a minimal surface roughness. The substrates were cleaned in acetone and then isopropanol in an ultrasonic bath and dried with compressed, dry air before loading to the deposition chamber. The base pressure in the main chamber prior to deposition was  $5.3 \times 10^{-6} \text{ Pa}$  or lower. The 4-inch diameter targets of Ir (99.9%, EvoChem, Germany), Ru (99.95%, EvoChem, Germany), and Ti (99.995%, FHR, Germany) were precleaned by sputtering with closed shutters prior to deposition. Ar (99.9999%) was used as the sputter gas and the pressure in the chamber was adjusted to 0.67 Pa at room temperature. A 20 nm Ti adhesion layer was deposited at 200 W RF with a constant substrate rotation of 20 rpm, in order to produce a uniform layer thickness from the confocal cathode arrangement. Next, the power applied to each cathode was independently

adjusted to yield the desired composition gradient ranges. Due to the confocal cathode arrangement and the cathode tilt with respect to the substrate surface, thickness gradients are produced when the substrate is static. As a result, the composition ratio of the co-sputtered elements in the mixture is dependent on the position on the sample surface, resulting in a combinatorial materials library. The resulting thickness of the obtained coating was approximately 250 nm in the substrate center. Thus, even at the thinnest point, there will always be greater than 100 nm thickness of material.

The composition of the obtained libraries was confirmed using EDX mapping (INCA X-act, Oxford Instruments, U.K.). Figure 6 shows the composition range of two Ru-Ir-Ti thin film libraries covering the investigated ternary alloys as assessed by EDX. For verifying the surface composition of the libraries, X-ray photoelectron spectroscopy (XPS) was employed, considering that the EDX data results from the whole volume of the film and only serves for estimation. Additionally, the Ti amount in Figure 6 is overestimated, since signals from the Ti adhesion layer contribute to those from the overlying Ru-Ir-Ti thin films. The XPS measurements were performed using a Quantera II (Physical Electronics, Chanhassen, MN, USA) device, equipped with a monochromatic Al  $K\alpha$ -X-ray source (1486.6 eV), which was operated at 15 kV and 25 W. Analysis of the spectra was carried out using the software Casa XPS (<http://www.casaxps.com/>). The exact surface compositions of the selected spots on the material libraries were determined by integration of the Ir  $4f_{7/2}$ , Ru  $3d_{5/2}$  and Ti  $2p_{3/2}$  peaks using corresponding relative sensitivity factors. The compositions of the electrodes are shown in Ir, Ru and Ti atomic compositions, omitting oxygen. A Gaussian-Lorentzian function was used to fit the contributions of lattice oxygen, OH-groups and  $H_2O$  molecules in the O 1s spectra.

A scanning flow cell (SFC) was connected to the inductively coupled plasma mass spectrometer (ICP-MS) to investigate catalytic activity and stability of different alloy compositions at the same time (online ICP-MS). The Ru-Ir-Ti thin film libraries were used as the working electrodes, of which the geometric surface area is defined by the circular port of the SFC (about 0.01 cm<sup>2</sup>). Mounted upstream in the inlet duct of the SFC, a graphite rod served as counter electrode. A conventional Ag/AgCl/3 M KCl electrode (Metrohm, Germany), connected with the outlet duct, downstream of the SFC, was employed as reference electrode. All SFC components, gas flow and the potentiostat (Gamry Reference [600],

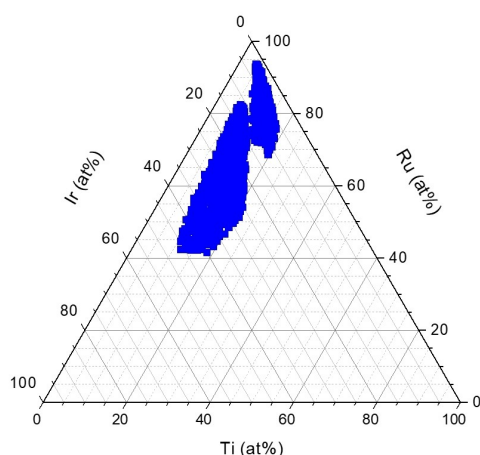


**Figure 6.** Composition diagrams of the investigated Ru-Ir-Ti thin film libraries, as quantified by Energy-Dispersive X-ray Spectroscopy (EDX). Please note, that the quantification of Ti content by EDX is overestimated due to contributions of Ti from the adhesion layer. The surface compositions have been verified using X-ray photoelectron spectroscopy (XPS).

USA) were controlled by homemade LabVIEW software (National Instruments, USA). Fresh 0.1 M  $HClO_4$  solution, prepared directly before the measurements by dilution of  $HClO_4$  (70%, Merck, Germany) in ultrapure water (18 m $\Omega$ cm, TOC < 3 ppb), was used as electrolyte for all electrochemical measurements. Before the measurements, the reversible hydrogen electrode (RHE) potential was measured on Pt thin films with an  $H_2$  saturated electrolyte against the Ag/AgCl/3 M KCl reference electrode. Accordingly, the RHE scale is used to present all potentials published in this work. During the electrochemical measurements, the electrolyte was saturated with Ar and pumped at a rate of about 205  $\mu$ L  $min^{-1}$  towards the ICP-MS (NexION 350X, Perkin Elmer, USA). Before flowing into the ICP-MS, the electrolyte was mixed with an internal standard in a 1:1 mixing ratio, using a Y-connector. With a concentration of the internal standard equal to 5  $\mu$ g  $L^{-1}$ , 5  $\mu$ g  $L^{-1}$  and 10  $\mu$ g  $L^{-1}$ , the intensities of the isotopes  $^{45}Sc$ ,  $^{103}Rh$  and  $^{187}Re$  were measured during the detection of  $^{55}Ti$ ,  $^{102}Ru$  and  $^{193}Ir$ , to ensure stable performance of the ICP-MS. The ICP-MS was calibrated each day before the measurements. For stabilization of the working electrode surface, the samples were polarized at 1.20  $V_{RHE}$  for 2 min before conducting the electrochemical protocol. The electrochemical protocol comprised an initial potential sweep at 10  $mV s^{-1}$  from 1.20  $V_{RHE}$  to a potential corresponding to a current density of 5  $mA cm^{-2}$ . Subsequently, the sample was anodically polarized at a current density of 1  $mA cm^{-2}$  for 2 min. Finally, the potential sweep was repeated, to investigate alterations before and after polarization. The potential required for reaching a current density of 5  $mA cm^{-2}$  was used as an activity descriptor to relate the electrochemical data to previous works. All measurements were conducted at least three times for each composition, to test reproducibility.

For performance testing on a longer time scale, three representative alloy composition were anodically polarized at 25  $mA cm^{-2}$  for about 28 h in an H-cell with anodic and cathodic compartments separated by a fine glass frit. Both compartments were filled with the electrolyte (each 30 mL of 0.1 M  $HClO_4$  solution). The sample, serving as working electrode, was submerged into the anodic compartment next to the reference electrode (Ag/AgCl/3 M KCl). A Pt thin film was used as counter electrode and was submerged into the cathodic compartment. During polarization, liquid samples of 1 mL volume were taken periodically from the anodic compartment, diluted 1:5 and analyzed by ICP-MS (NexION 350X, Perkin Elmer, USA). To maintain a constant volume, the compartment was replenished with fresh electrolyte after each sampling step. To account for possible diffusion/migration of dissolved species through the glass frit, a liquid sample from the cathodic compartment was taken after the experiment. Only traces of Ir, Ru and Ti were detected at the cathode, still the dissolution profiles were corrected for these values.

## Acknowledgements

LL and OK acknowledge financial support from the Helmholtz Networking and Initiative Fund. OK greatly acknowledges support from the German Federal Ministry of Education and Research in the framework of the project CatLab (03EW0015A/B). OK acknowledges funding from the German Research Foundation (DFG) – Project-ID 431791331 – SFB 1452. Open Access funding enabled and organized by Projekt DEAL.

## Conflict of Interests

The authors declare no conflict of interest.

## Data Availability Statement

The data that support the findings of this study are available from the corresponding author upon reasonable request.

**Keywords:** catalyst stability · oxygen evolution reaction · Ru-Ir-Ti alloy · thin film catalyst · online ICP-MS

- [1] P. Sorensen, N. A. Cutululis, A. Viguera-Rodriguez, L. E. Jensen, J. Hjerrild, M. H. Donovan, H. Madsen, *IEEE Trans. Power Appar. Syst.* **2007**, *22*, 958–965.
- [2] A. Virtuani, L. Fanni, *Prog. Photovoltaics* **2014**, *22*, 208–217.
- [3] Y. Matsumoto, E. Sato, *Mater. Chem. Phys.* **1986**, *14*, 397–426.
- [4] E. Fabbri, A. Haberer, K. Waltar, R. Kotz, T. J. Schmidt, *Catal. Sci. Technol.* **2014**, *4*, 3800–3821.
- [5] J. Rossmeisl, A. Logadottir, J. K. Nørskov, *Chem. Phys.* **2005**, *319*, 178–184.
- [6] M. Carmo, D. L. Fritz, J. Mergel, D. Stolten, *Int. J. Hydrogen Energy* **2013**, *38*, 4901–4934.
- [7] S. Trasatti, *Electrochim. Acta* **1984**, *29*, 1503–1512.
- [8] Y. Kamegaya, K. Sasaki, M. Oguri, T. Asaki, H. Kobayashi, T. Mitamura, *Electrochim. Acta* **1995**, *40*, 889–895.
- [9] O. Kasian, S. Geiger, P. Stock, G. Polymeros, B. Breitbach, A. Savan, A. Ludwig, S. Cherevko, K. J. J. Mayrhofer, *J. Electrochem. Soc.* **2016**, *163*, F3099–F3104.
- [10] S. Cherevko, S. Geiger, O. Kasian, N. Kulyk, J. P. Grote, A. Savan, B. R. Shrestha, S. Merzlikin, B. Breitbach, A. Ludwig, K. J. J. Mayrhofer, *Catal. Today* **2016**, *262*, 170–180.
- [11] J. Rossmeisl, Z.-W. Qu, H. Zhu, G.-J. Kroes, J. K. Nørskov, *J. Electroanal. Chem.* **2007**, *607*, 83–89.
- [12] I. C. Man, H. Y. Su, F. Calle-Vallejo, H. A. Hansen, J. I. Martínez, N. G. Inoglu, J. Kitchin, T. F. Jaramillo, J. K. Nørskov, J. Rossmeisl, *ChemCatChem* **2011**, *3*, 1159–1165.
- [13] T. Reier, M. Oezaslan, P. Strasser, *ACS Catal.* **2012**, *2*, 1765–1772.
- [14] N. Danilovic, R. Subbaraman, K. C. Chang, S. H. Chang, Y. Kang, J. Snyder, A. P. Paulikas, D. Strmcnik, Y. T. Kim, D. Myers, *Angew. Chem.* **2014**, *126*, 14240–14245.
- [15] S. Cherevko, S. Geiger, O. Kasian, A. Mingers, K. J. Mayrhofer, *J. Electroanal. Chem.* **2016**, *773*, 69–78.
- [16] S. Cherevko, S. Geiger, O. Kasian, A. Mingers, K. J. Mayrhofer, *J. Electroanal. Chem.* **2016**, *774*, 102–110.
- [17] S. Cherevko, A. R. Zeradjanin, A. A. Topalov, N. Kulyk, I. Katsounaros, K. J. J. Mayrhofer, *ChemCatChem* **2014**, *6*, 2219–2223.
- [18] R. Kötzt, S. Stucki, *J. Electrochem. Soc.* **1985**, *132*, 103.
- [19] R. Kötzt, S. Stucki, *Electrochim. Acta* **1986**, *31*, 1311–1316.
- [20] V. A. Saveleva, L. Wang, W. Luo, S. Zafeiratos, C. Ulhaq-Bouillet, A. S. Gago, K. A. Friedrich, E. R. Savinova, *J. Phys. Chem. Lett.* **2016**, *7*, 3240–3245.
- [21] G. Li, H. Yu, W. Song, X. Wang, Y. Li, Z. Shao, B. Yi, *Int. J. Hydrogen Energy* **2012**, *37*, 16786–16794.
- [22] L.-E. Owe, M. Tsyppkin, K. S. Wallwork, R. G. Haverkamp, S. Sunde, *Electrochim. Acta* **2012**, *70*, 158–164.
- [23] J. Cheng, H. Zhang, G. Chen, Y. Zhang, *Electrochim. Acta* **2009**, *54*, 6250–6256.
- [24] A. T. Marshall, R. G. Haverkamp, *Electrochim. Acta* **2010**, *55*, 1978–1984.
- [25] W. Du, N. A. Deskins, D. Su, X. Teng, *ACS Catal.* **2012**, *2*, 1226–1231.
- [26] J. M. Roller, M. J. Arellano-Jiménez, R. Jain, H. Yu, C. B. Carter, R. Maric, *J. Electrochem. Soc.* **2013**, *160*, F716.
- [27] O. Kasian, J. P. Grote, S. Geiger, S. Cherevko, K. J. J. Mayrhofer, *Angew. Chem. Int. Ed.* **2018**, *57*, 2488–2491.
- [28] O. Kasian, S. Geiger, T. Li, J.-P. Grote, K. Schweinar, S. Zhang, C. Scheu, D. Raabe, S. Cherevko, B. Gault, *Energy Environ. Sci.* **2019**, *12*, 3548–3555.
- [29] P. Jovanović, N. Hodnik, F. Ruiz-Zepeda, I. Arčon, B. Jozinović, M. Zorko, M. Bele, M. Šala, V. S. Šelih, S. Hočevar, *J. Am. Chem. Soc.* **2017**, *139*, 12837–12846.
- [30] J. Xu, G. Liu, J. Li, X. Wang, *Electrochim. Acta* **2012**, *59*, 105–112.
- [31] E. Balko, P. Nguyen, *J. Appl. Electrochem.* **1991**, *21*, 678–682.
- [32] M. Ledendecker, S. Geiger, K. A. Hengge, J. Lim, S. Cherevko, A. M. Mingers, D. Göhl, G. V. Fortunato, D. Jalalpoor, F. Schüth, *Nano Res.* **2019**, *12*(9), 2275–2280.
- [33] S. Ferro, D. Rosestolato, C. A. Martínez-Huitle, A. De Battisti, *Electrochim. Acta* **2014**, *146*, 257–261.
- [34] O. Kasian, T. Li, A. M. Mingers, K. Schweinar, A. Savan, A. Ludwig, K. Mayrhofer, *J. Phys. Energy* **2021**, *3*, 034006.
- [35] S. Fierro, T. Nagel, H. Baltruschat, C. Comninellis, *Electrochem. Commun.* **2007**, *9*, 1969–1974.
- [36] G. Li, K. Li, L. Yang, J. Chang, R. Ma, Z. Wu, J. Ge, C. Liu, W. Xing, *ACS Appl. Mater. Interfaces* **2018**, *10*, 38117–38124.
- [37] M. Bernt, H. A. Gasteiger, *J. Electrochem. Soc.* **2016**, *163*, F3179.
- [38] R. Hutchings, K. Müller, R. Kötzt, S. Stucki, *J. Mater. Sci.* **1984**, *19*, 3987–3994.
- [39] R. Yeo, J. Orehtsky, W. Visscher, S. Srinivasan, *J. Electrochem. Soc.* **1981**, *128*, 1900.
- [40] V. Gorodetskii, V. Neburchilov, *Russ. J. Electrochem.* **2007**, *43*, 223–228.
- [41] V. Gorodetskii, V. Neburchilov, *Russ. J. Electrochem.* **2003**, *39*, 1111–1115.
- [42] V. Gorodetskii, V. Neburchilov, V. Alyab'eva, *Russ. J. Electrochem.* **2005**, *41*, 1111–1117.
- [43] S. Barison, S. Daolio, M. Fabrizio, A. D. Battisti, *Rapid Commun. Mass Spectrom.* **2004**, *18*, 278–284.
- [44] S. Barison, A. De Battisti, M. Fabrizio, S. Daolio, C. Piccirillo, *Rapid Commun. Mass Spectrom.* **2000**, *14*, 2165–2169.
- [45] S. Hoseinie, F. Ashrafzadeh, M. Maddahi, *J. Electrochem. Soc.* **2010**, *157*, E50.
- [46] V. Gorodetskii, V. Neburchilov, *Russ. J. Electrochem.* **2003**, *39*, 1116–1123.
- [47] V. Gorodetskii, V. Neburchilov, V. Alyab'eva, *Russ. J. Electrochem.* **2005**, *41*, 964–970.
- [48] V. Gorodetskii, V. Neburchilov, *Russ. J. Electrochem.* **2005**, *41*, 971–978.
- [49] R. Kötzt, H. Lewerenz, P. Brüesch, S. Stucki, *J. Electroanal. Chem. Interfacial Electrochem.* **1983**, *150*, 209–216.
- [50] L. Da Silva, V. Alves, S. De Castro, J. Boodts, *Colloids Surf. A* **2000**, *170*, 119–126.
- [51] J. Augustynski, M. Koudelka, J. Sanchez, B. Conway, *J. Electroanal. Chem. Interfacial Electrochem.* **1984**, *160*, 233–248.
- [52] H. Lewerenz, S. Stucki, R. Kötzt, *Surf. Sci.* **1983**, *126*, 463–468.
- [53] J. Shen, A. Adnot, S. Kaliaguine, *Appl. Surf. Sci.* **1991**, *51*, 47–60.
- [54] M. Kuznetsov, J. F. Zhuravlev, V. Gubanov, *J. Electron Spectrosc. Relat. Phenom.* **1992**, *58*, 169–176.
- [55] S. Gottesfeld, S. Srinivasan, *J. Electroanal. Chem. Interfacial Electrochem.* **1978**, *86*, 89–104.
- [56] V. Birss, R. Myers, H. Angerstein-Kozłowska, B. Conway, *J. Electrochem. Soc.* **1984**, *131*, 1502.
- [57] D. Čukman, M. Vuković, *J. Electroanal. Chem. Interfacial Electrochem.* **1990**, *279*, 283–290.
- [58] D. N. Buckley, L. D. Burke, *J. Chem. Soc. Faraday Trans. 1* **1975**, *71*, 1447–1459.
- [59] A. Minguzzi, O. Lugaresi, E. Achilli, C. Locatelli, A. Vertova, P. Ghigna, S. Rondinini, *Chem. Sci.* **2014**, *5*, 3591–3597.
- [60] D. N. Buckley, L. D. Burke, *J. Chem. Soc. Faraday Trans. 1* **1976**, *72*, 2431–2440.
- [61] M. Miles, E. Klaus, B. Gunn, J. Locker, W. Serafin, S. Srinivasan, *Electrochim. Acta* **1978**, *23*, 521–526.
- [62] S. Trasatti, G. Buzzanca, *J. Electroanal. Chem. Interfacial Electrochem.* **1971**, *29*, A1–A5.
- [63] D. Galizzioli, F. Tantardini, S. Trasatti, *J. Appl. Electrochem.* **1974**, *4*, 57–67.
- [64] D. Galizzioli, F. Tantardini, S. Trasatti, *J. Appl. Electrochem.* **1975**, *5*, 203–214.
- [65] N. Hodnik, P. Jovanović, A. Pavlišić, B. Jozinović, M. Zorko, M. Bele, V. S. Šelih, M. Šala, S. Hočevar, M. Gaberšek, *J. Phys. Chem. C* **2015**, *119*, 10140–10147.
- [66] A. R. Zeradjanin, N. Menzel, P. Strasser, W. Schuhmann, *ChemSusChem* **2012**, *5*, 1897–1904.
- [67] R. Kötzt, H. Lewerenz, S. Stucki, *J. Electrochem. Soc.* **1983**, *130*, 825.
- [68] C. Angelinetta, S. Trasatti, L. D. Atanososka, R. T. Atanososki, *J. Electroanal. Chem. Interfacial Electrochem.* **1986**, *214*, 535–546.
- [69] S. Siracusano, N. Hodnik, P. Jovanovic, F. Ruiz-Zepeda, M. Šala, V. Baglio, A. S. Aricò, *Nano Energy* **2017**, *40*, 618–632.
- [70] A. Loncar, L. Moriau, K. Stojanovski, F. Ruiz-Zepeda, P. Jovanovic, M. Bele, M. Gaberšek, N. Hodnik, *J. Phys. Energy* **2020**, *2*, 02LT01.

- [71] C. Van Pham, M. Bühler, J. Knöppel, M. Bierling, D. Seeberger, D. Escalera-López, K. J. Mayrhofer, S. Cherevko, S. Thiele, *Appl. Catal. B* **2020**, *269*, 118762.
- [72] E. Oakton, D. Lebedev, M. Povia, D. F. Abbott, E. Fabbri, A. Fedorov, M. Nachtegaal, C. Copéret, T. J. Schmidt, *ACS Catal.* **2017**, *7*, 2346–2352.
- [73] K. Kameyama, K. Tsukada, K. Yahikozawa, Y. Takasu, *J. Electrochem. Soc.* **1994**, *141*, 643.
- [74] M. T. Koper, *J. Electroanal. Chem.* **2011**, *660*, 254–260.
- [75] R. Kötz, H. Neff, S. Stucki, *J. Electrochem. Soc.* **1984**, *131*, 72.
- [76] J. Chastain, R. C. King Jr, *Perkin-Elmer Corporation* **1992**, *40*, 221.
- [77] D. Escalera-López, S. Czioska, J. Geppert, A. Boubnov, P. Röse, E. Saraçi, U. Krewer, J.-D. Grunwaldt, S. Cherevko, *ACS Catal.* **2021**, *11*, 9300–9316.
- [78] S. Geiger, O. Kasian, M. Ledendecker, E. Pizzutilo, A. M. Mingers, W. T. Fu, O. Diaz-Morales, Z. Li, T. Oellers, L. Fruchter, *Nat. Catal.* **2018**, *1*, 508–515.
- [79] O. Kasian, S. Geiger, K. J. Mayrhofer, S. Cherevko, *Chem. Rec.* **2019**, *19*, 2130–2142.
- [80] N. Danilovic, R. Subbaraman, K.-C. Chang, S. H. Chang, Y. J. Kang, J. Snyder, A. P. Paulikas, D. Strmcnik, Y.-T. Kim, D. Myers, *J. Phys. Chem. Lett.* **2014**, *5*, 2474–2478.

---

Manuscript received: August 9, 2023

Revised manuscript received: November 2, 2023

Version of record online: November 30, 2023